IEEE Access
Multidisciplinary | Rapid Review | Open Access Journal

Received 9 October 2022, accepted 24 October 2022, date of publication 31 October 2022, date of current version 4 November 2022.

Digital Object Identifier 10.1109/ACCESS.2022.3218325

RESEARCH ARTICLE

The Hall Sensors Fault-Tolerant for PMSM Based on Switching Sensorless Control With PI Parameters Optimization

YI HUANG, MI ZHAO, JIAN ZHANG, AND MIN LU
College of Mechanical and Electrical Engineering, Shihezi University, Shihezi 832003, China

Corresponding author: Mi Zhao (zhaomi530@163.com)

This work was supported in part by the Natural Science Foundation of China under Grant 61563045, and in part by the International Cooperation Projects of Shihezi University under Grant GJHZ202003.

ABSTRACT The failure of Hall sensors can give rise to loss of rotor position and speed information, which can result in loss of control of the speed loop, spatial decoupling errors, and affecting system stability in three-phase permanent magnet synchronous motor (PMSM) control system. To solve this problem, a Hall fault-tolerant control system based on sensorless state switching is proposed in this paper. Firstly, a three-phase PMSM control system based on field oriented control (FOC) is established to analyze and clarify the importance of rotor position and speed signals. Secondly, a detection scheme based on Hall change edge signal is designed to detect the health status of Hall sensors and implement fault-tolerant state switching. For the stability of the system, a sliding mode observer (SMO) is built to obtain the back electromotive force (back-EMF). In addition, the phase-locked loop (PLL) is designed to extract the rotor position and speed information from the back-EMF. When the system enters a fault-tolerant state, changes in the speed feedback loop can affect the control performance of the system. Therefore, the speed loop PI parameter optimization scheme based particle swarm optimization (PSO) algorithm is proposed to optimize the performance of the fault tolerant control system. Finally, the effectiveness of the fault-tolerant method based on the sensorless state switching after particle swarm optimization is verified on a semi-physical platform (RCP-HIL). The experimental results show that the Hall fault-tolerant control system proposed in this paper can effectively detect Hall sensor faults and cut into the fault-tolerant control state, and can maintain the control system stable during fault-tolerant state switching. Furthermore, the control system can maintain an observation error of $\pm 30rpm$ under variable load or variable speed conditions at medium and high speeds when the system enters fault-tolerant control state.

INDEX TERMS PMSM, hall sensors, fault tolerance control, sliding mode observer, particle swarm optimization.

I. INTRODUCTION

The permanent magnet synchronous motor (PMSM) with simple structure, easy control, high interference immunity and high energy efficiency has been widely applied in various fields such as industrial processing, automobile drive and aerospace [1], [2], [3], [4]. To achieve precise control of PMSM, the classical strategies of field-oriented, direct torque and predictive control all require to obtain accurate rotor position and speed information. Among them, the Hall sensor is widely adopted to obtain the rotor position and speed signals of the motor because of its simple installation and low price [5]. However, Hall sensors are easily damaged by environmental and magnetic field changes (such as high temperature, low temperature, pollution, vibration and strong magnetic field, *etc.*) in practical applications. If there is an error in obtaining location information, especially in cranes, elevators and other equipment, immeasurable losses can be

The associate editor coordinating the review of this manuscript and approving it for publication was Kan Liu.

caused [6], [7]. Therefore, it is of practical significance to design a fault-tolerant control method for Hall sensor faults in the commonly used three-phase PMSM.

In order to accurately detect the health condition of Hall sensors, many detection methods have been proposed, including time-based and signal coding-based methods and so on. In [8], scholars achieve the detection of the health status of Hall sensors by comparing the phase difference of the Hall-encoded signals after CLARK transformation. Although this method achieves online fault detection by phase difference, it brings a large amount of computation during vector transformation, which puts a large burden on CPU that adopts fixed-point computation. A dual Hall sensors device is utilized to implement sensor fault detection and fault-tolerant control, which provides better error suppression for both load variations and noise disturbances [9]. However, the solution of hardware redundancy significantly increases the size and cost of the device. Besides, some detection methods based on Hall signal switching time and Hall coding information have been proposed in [10] and [11], which can achieve fault detection through simple calculations. However, the time-based detection method has a certain error in variable speed. Therefore, the detection scheme based on Hall-coded information has a greater practical value.

Nowadays, a few of sensorless algorithms are also applied for situations where the rotor position is faulty or the sensor cannot be installed. The sensorless control algorithms are mainly classified into model-based and signal injection-based approaches [12], [13], [14], [15]. Among them, model-based methods have superior performance at medium and high speeds, while signal injection-based methods are more advantageous at low and zero speeds [16], [17], [18], [19], [20]. Sliding mode observer (SMO) is widely applied in medium and high-speed applications because of its strong robustness, anti-parameter perturbation and fast response among many schemes of sensorless control [21], [22], [23], [24]. Therefore, it has great advantages to design a fault-tolerant control system under the fault of Hall position sensor based on the sensorless control strategy of SMO. In addition, some scholars have also carried out corresponding research on the optimization of the controller parameters in the motor control system [25], [26]. Therefore, it is necessary to point out that the parameter mismatch caused by the switching of the system control state deserves further consideration, which is very valuable for maintaining the stability of the control system.

Inspired by the above discussion, this paper proposes a fault detection scheme for Hall sensor based on the encoded signals of Hall jump edges to achieve fault detection and fault-tolerant control switching. Secondly, a fault-tolerant control method for Hall sensor based on control state switching is proposed. On the one hand, the method utilizes a sensorless scheme based on a SMO as a fault tolerance mechanism for medium and high speeds. On the other hand, a scheme of controller parameter optimization based on particle swarm optimization (PSO) is designed to solve the problem of speed controller parameter mismatch during sensorless state switching.

The rest of this paper is organized as follows. Section II presents the mathematical model of PMSM and the structure of the control system under the conventional field oriented control (FOC) strategy. In Section III, a fault-tolerant control system based on a mode of sensorless control state switching is proposed and designed. In Section IV, the proposed fault-tolerant control system is experimented and verified in a semi-physical simulation platform for the observer response speed and accuracy, control system variable load response performance and variable speed performance when the system enters the fault-tolerant control state, respectively. Finally, Section V concludes the article.

II. THE DESIGN OF FAULT-TOLERANT CONTROL SYSTEM FOR THREE-PHASE PMSM

In order to develop the fault-tolerant control algorithm for the position sensor failure of three-phase PMSM, the star-connected surface permanent magnet synchronous motor (SPMSM) is selected as the research object in this paper. The following assumptions are made for the controlled object to facilitate the analysis [27].

1) The magnetic saturation effect of the motor iron core is not considered.
2) The eddy current and hysteresis losses caused by the magnetic circuit of the motor are ignored.
3) The physical parameters of the stator windings of each phase are the same, and the distribution of the excitation magnetic field generated by the rotor is a standard sine wave.
4) The cogging effect of the motor is ignored.
5) The effects of the inverter's freewheeling diode voltage drop, switching time and dead-time effects are ignored.

There is no doubt that the stable control performance of the three-phase PMSM control system requires the accurate acquisition of accurate position signals and speed signals by the Hall sensor. However, the accuracy and reliability of Hall sensors are susceptible to harsh environments and strong magnetic fields. Consequently, a fault-tolerant control system based on a SMO using the parameters measured in the system is designed to solve the problem of Hall sensor failure during motor operation in this paper. The block diagram of the fault-tolerance system is shown in Fig.1.

From Fig.1, the whole system mainly includes the classical control FOC module, fault-tolerant control module and parameter optimization module. Among them, the whole control framework of FOC mainly consists of modules such as speed regulator (ASR), current regulator (ACR), inverter, PMSM and Hall sensor. In FOC framework, conventional PI controllers are used for both speed and current controllers. Meanwhile, the control strategy of "$i_{d\_ref} = 0$" is applied in the control framework of FOC in order to obtain the maximum torque benefit. Secondly, the fault-tolerant control system applies a fault detection module of Hall sensor to

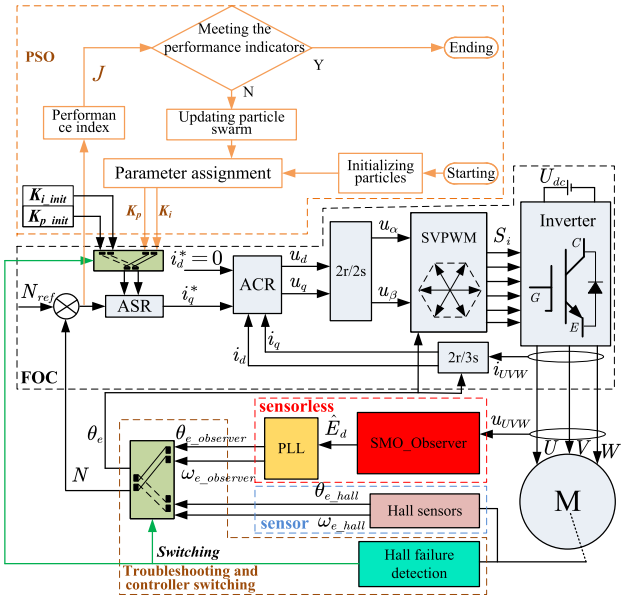

FIGURE 1. The block diagram of Hall fault-tolerant control system based on sensorless state switching after particle swarm optimization.

determine the health status of the position sensor, which controls the system to switch from the sensor state to the sensorless state. Furthermore, a program based on phase-locked loop (PLL) and SMO is designed to obtain rotor information in a senseless state. Finally, a parameter optimization module based PSO is utilized to optimize the parameters of the ASR when the system is switched to the sensorless state.

A. THE FAULT DETECTION OF HALL SENSORS

The detection of the health state in Hall sensor is the key to the fault-tolerant control system. In this paper, the traditional single-phase Hall fault is analyzed (the way to obtain rotor information is quickly switched after the fault to avoid the impact of the remaining Hall fault again). The coded information from the Hall output is employed for fault status detection. Under normal conditions, the coding sequence of three-phase Hall in one cycle (T) is shown by Fig.2.

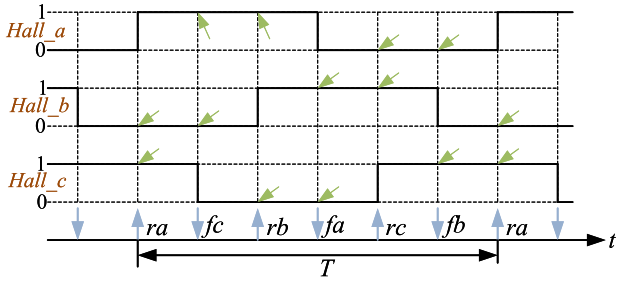

FIGURE 2. The normal Hall coding sequence.

From Fig.2, it is clear that a complete electrical cycle consists of six sectors. Usually, the scheme of interpolation is utilized to perform rotor position estimation to improve the resolution of the sensor. Therefore, the method of M/T is used to calculate the rotor speed. The calculation principle is shown in Eq.(1).

$$n = \frac{F_0 M_0}{C M_1} \tag{1}$$

where, n is the speed. M_0 indicates the encoder count value per unit time. M_1 indicates the number of pulses of known frequency sent per counting moment. C indicates the count value of one cycle, respectively. On this basis, the rotor position at t_k can be calculated from the rotor speed and rotor position at t_{k-1}. The Hall-encoded sequence is shown in Tab.1.

TABLE 1. Hall-encoded sequence in one cycle (T).

Hall_a	1	1	1	0	0	0
Hall_b	0	0	1	1	1	0
Hall_c	1	0	0	0	1	1

In Fig.2, *ra*, *fc*, *rb*, *fa*, *rc*, and *fb* represent each Hall state change moment, where *r* and *f* denote the rising and falling edges of the signal, respectively. Moreover, "0" and "1" are Hall output level states. According to the correct coding sequence, it is clear that the remaining two phases of Hall can output opposite levels when the same Hall output signal is at different jump edges (e.g. *ra* and *fa*). Based on the above encoding law of Hall jump edge, the state equation of Hall jump edge is defined as Eq.(2).

$$State\_hall\_i = |test(fj, i) - test(rj, i)|; \quad (i, j = a, b, c) \tag{2}$$

In Eq.(2), $State\_hall\_i$ shows the health status indicator of phase *i* Hall, and the normal case is 1. $test(rj, i)$ and $test(fj, i)$ indicate the level states of phase *i* Hall outputs at rising and falling edges of phase *j* Hall, respectively. It can be seen that Eq.(2) is unique to the determination of Hall state. Furthermore, the case of a single-phase Hall fault can be briefly analyzed by Fig.3. If A-phase Hall fails at the moment t_f, A-phase Hall will miss the edge change and only maintain a constant output (output sets to "1" or "0").

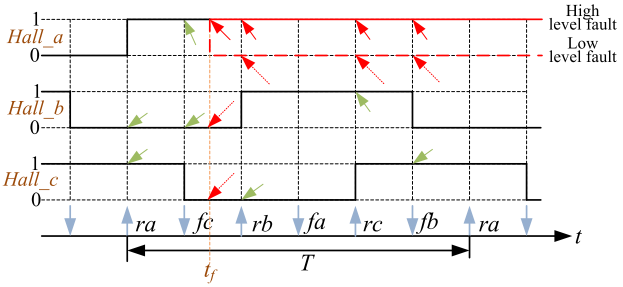

FIGURE 3. The phase A Hall fault coding sequence.

When A-phase Hall fails, the three-phase Hall output state codes are shown in Tab.2. If there is a zero-setting fault (a new jumping edge) in A-phase Hall, its health state indicator can

TABLE 2. Hall coding sequence in phase A Hall fault state.

Time	*ra*	*fc*	*tf*	*rb*	*fa*	*rc*	*fb*
Hall_a	1	1	1	1	1	1	1
			0	0	0	0	0
Hall_b	0	0	1	1	1	1	0
HaLL_c	1	0	0	0	0	1	1

be calculated as 0 by Eq.(3), which determines in that there is a Hall fault. If A-phase Hall has a fault of setting "1" (no new jump edge), the equation of jump edge state is deactivated at this time since the next jump edge signal is not available. However, it is possible to determine that there is a Hall fault by the equation of state along the jump of the remaining Hall (C-phase Hall), which can ensure the fastest judgment speed in 2/3 electrical cycle (T).

$$\begin{aligned} State\_hall\_a &= |test\ (fb, a) - test\ (rb, a)| \\ &= |test\ (fc, a) - test\ (rc, a)| = 0 \end{aligned} \tag{3}$$

The above fault states can be extended to any Hall, which enables the detection of Hall fault states. As soon as a fault message is detected ($State\_hall\_a = 0$), the fault detection module outputs a signal to switch the rotor position signal acquisition path. This means that the system cuts to a fault-tolerant control state and the angular and rotor information needed by the controller be provided by the sensorless observer when a faulty Hall fault is effectively detected. Moreover, the speed loop parameters are also switched to optimized parameters in case of Hall failure to avoid system instability due to changes in the speed feedback loop.

However, this method currently does not accurately locate the location of the faulty Hall. To locate specifically, the fault location should be achieved by combining the coded information of multiple fault signals.

B. THE DESIGN OF SLIDING MODE OBSERVER

According to the voltage and current equations of PMSM in the synchronous rotating coordinate system, as shown in Eqs.(4) and (5), it can be obtained that the back-EMF contains rotor information in the steady state, which can be accurately observed by designing a SMO.

$$\begin{bmatrix} u_d \\ u_q \end{bmatrix} = \begin{bmatrix} R + L_d p & -\omega_e L_q \\ \omega_e L_q & R + L_q p \end{bmatrix} \begin{bmatrix} i_d \\ i_q \end{bmatrix} + \begin{bmatrix} 0 \\ \omega_e \psi_f \end{bmatrix} \tag{4}$$

$$\begin{bmatrix} pi_d \\ pi_q \end{bmatrix} = \begin{bmatrix} -\dfrac{R}{L_d} & \dfrac{\omega_e L_q}{L_d} \\ -\dfrac{\omega_e L_d}{L_q} & -\dfrac{R}{L_q} \end{bmatrix} \begin{bmatrix} i_d \\ i_q \end{bmatrix} + \begin{bmatrix} \dfrac{u_d}{L_d} \\ \dfrac{u_q - \omega_e \psi_f}{L_q} \end{bmatrix} \tag{5}$$

In Eqs.(4) and (5), p is the differential operator. i_d, u_d and L_d are the d-axis equivalent current, voltage and inductance, respectively. R is the equivalent stator resistance in the synchronous rotating coordinate system. ω_e is the electrical angular velocity, and ψ_f is the permanent magnet flux linkage.

The current equation is rewritten as Eq.(6) by introducing the the back-EMF (E_d, E_q) of dq-axis.

$$\begin{bmatrix} pi_d \\ pi_q \end{bmatrix} = \begin{bmatrix} -\dfrac{R}{L_d} & \dfrac{L_q \omega_e}{L_d} \\ -\dfrac{L_d \omega_e}{L_q} & -\dfrac{R}{L_q} \end{bmatrix} \begin{bmatrix} i_d \\ i_q \end{bmatrix} + \begin{bmatrix} \dfrac{u_d - E_d}{L_d} \\ \dfrac{u_q - E_q}{L_q} \end{bmatrix} \tag{6}$$

In Eq.(6), $E_q = \omega_e \psi_f$. When the d-axis current expectation is set to 0, $E_d = 0$ is satisfied in the steady-state system. To obtain the back-EMF of dq-axis accurately, the observer equation in the synchronous rotating coordinate system is established according to the current equation, as shown in Eq.(7) [28].

$$\begin{bmatrix} p\hat{i}_d \\ p\hat{i}_q \end{bmatrix} = \begin{bmatrix} -\dfrac{R}{L_d} & \dfrac{L_q \omega_e}{L_d} \\ -\dfrac{L_d \omega_e}{L_q} & -\dfrac{R}{L_q} \end{bmatrix} \begin{bmatrix} \hat{i}_d \\ \hat{i}_q \end{bmatrix} + \begin{bmatrix} \dfrac{u_d - \hat{E}_d}{L_d} \\ \dfrac{u_q - \hat{E}_q}{L_q} \end{bmatrix} \tag{7}$$

where $\hat{i}_d$, $\hat{i}_q$, $\hat{E}_d$ and $\hat{E}_q$ are the estimates of the current and voltage components in the dq-axis coordinate system, respectively. The back-EMF observation equation is designed by choosing the function of $sgn(x)$ such that the back-EMF under the dq-axis can be accurately observed.

$$\begin{bmatrix} \hat{E}_d \\ \hat{E}_q \end{bmatrix} = k \begin{bmatrix} sgn(\hat{i}_d - i_d) \\ sgn(\hat{i}_q - i_q) \end{bmatrix} \tag{8}$$

where k is the gain of the sliding mode observer. The observer error equation is established in Eq.(9) by subtracting Eq.(6) from Eq.(8).

$$\begin{bmatrix} p\tilde{i}_d \\ p\tilde{i}_q \end{bmatrix} = \begin{bmatrix} -\dfrac{R}{L_d} & \dfrac{L_q \omega_e}{L_d} \\ -\dfrac{L_d \omega_e}{L_q} & -\dfrac{R}{L_q} \end{bmatrix} \begin{bmatrix} \tilde{i}_d \\ \tilde{i}_q \end{bmatrix} + \begin{bmatrix} \dfrac{E_d - \hat{E}_d}{L_d} \\ \dfrac{E_q - \hat{E}_q}{L_q} \end{bmatrix} \tag{9}$$

In Eq.(9), $\tilde{i}_d$ and $\tilde{i}_q$ are the error value between the predicted and actual currents in the dq-axis, which can be specified in Eq.(10).

$$\begin{bmatrix} \tilde{i}_d \\ \tilde{i}_q \end{bmatrix} = \begin{bmatrix} \hat{i}_d - i_d \\ \hat{i}_q - i_q \end{bmatrix} \tag{10}$$

Finally, the error of observer is adopted to design the sliding surface in the dq-coordinate plane, as shown in Eq.(11), which ensures that the observation error is 0 after the observer converges to the sliding mode surface.

$$s = \begin{bmatrix} s_1 \\ s_2 \end{bmatrix} = \begin{bmatrix} \tilde{i}_d \\ \tilde{i}_q \end{bmatrix} = 0 \tag{11}$$

Generally, the stability of the observer can be proved by Lyapulov stability analysis. When the positive definite function is defined as Eq.(12). The sufficient condition for the stability of the observer can be derived as Eq.(13). Therefore,

the stability condition of the sliding mode observer is shown in Eq.(14).

$$s(x) = \frac{1}{2}s^2 \tag{12}$$

$$\lim_{s\to 0} s\dot{s} \le 0 \tag{13}$$

$$k > \max\{-R|\tilde{i}_d| + L_q\omega_e\tilde{i}_q sgn\left(\tilde{i}_d\right) + E_d sgn\left(\tilde{i}_d\right), -R|\tilde{i}_q| - L_d\omega_e\tilde{i}_d sgn\left(\tilde{i}_q\right) + E_q sgn\left(\tilde{i}_q\right)\} \tag{14}$$

From the perspective of a practical discrete controller, the observer equations require to be discretized. The inverse difference discretization result of the sliding mode observer equation is shown in Eqs.(15) and (16).

$$\begin{cases}\hat{i}_d(k+1) = A_d i_d(k) + B_d[u_d(k) + \omega_e L_q \hat{i}_q(k) - \hat{E}_d(k)] \\ \hat{i}_q(k+1) = A_q i_q(k) + B_q[u_q(k) + \omega_e L_d \hat{i}_d(k) - \hat{E}_q(k)]\end{cases} \tag{15}$$

$$\begin{cases}A_i = e^{-\frac{RT_s}{L_i}} \\ B_i = \dfrac{1}{L_s}\displaystyle\int_0^{T_s} e^{-\frac{RT_s}{L_i}} d\tau, \quad (i = d, q)\end{cases} \tag{16}$$

C. THE ROTOR POSITION AND SPEED ACQUISITION

Considering that the discontinuous term ($sgn(x)$) in the observer causes the observation value of back-EMF to contain high-frequency signals, there is a huge deviation in the speed value, when the d-axis back EMF is utilized, then the integral action further enlarges the error of the rotor position. Therefore, PLL is employed for efficient acquisition of rotor position and speed information. The voltage equation according to the observed electrical angle in the two-phase rotating coordinate system is derived in Eq.(17).

$$\begin{cases}V_d = u\cos(\hat{\theta}_e - \theta_e) = u\sin(\hat{\theta}_e - \theta_e + \dfrac{\pi}{2}) \\ V_q = u\cos(\hat{\theta}_e - \theta_e)\end{cases} \tag{17}$$

In Eq.(17), V_d and V_q are the equivalent voltages of the actual three-phase voltages in the synchronous rotating coordinate system, respectively. θ_e is the actual electrical angle of the rotor. When the system is in steady state, we have $E_d = 0$, then $E_d = V_d = \hat{E}_d$ is satisfied. Therefore, a PLL is established using the variable of d-axis to observe the speed and position of the motor rotor, as shown in Fig.4. When PLL converges, the observed electrical angle ($\hat{\theta}_e + \frac{\pi}{2}$) converges to the actual electrical angle (θ_e). Considering that

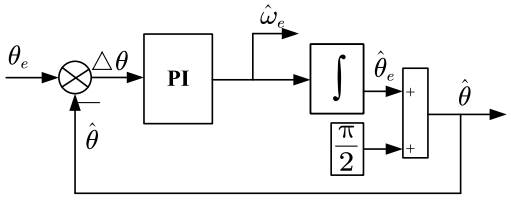

FIGURE 4. The schematic diagram of phase-locked loop based on d-axis back EMF.

$\Delta\theta$ is defined as the error of PLL and leting $\hat{\theta}_e + \frac{\pi}{2} = \hat{\theta}$, $\Delta\theta = \hat{\theta} - \theta_e = \sin(\Delta\theta)$ can be approximated when θ is between $-\frac{\pi}{6}$ and $\frac{\pi}{6}$.

D. THE PARAMETER OPTIMIZATION OF SPEED LOOP CONTROLLER BASED ON PSO

When a Hall fault is detected during the actual operation of the motor, the system directly utilizes an observer to obtain rotor position and speed information. Unfortunately, when the system is switched to an observer to obtain rotor position and speed signals, the speed loop can be mismatched with speed controller parameters due to changes in the feedback loop, which inevitably can result in reduced or even uncontrolled performance of the speed loop control. Therefore, the control parameters in speed loop should be further adjusted for better control performance.

Through the above analysis, a scheme based on the algorithm of particle swarm algorithm (PSO) to optimize the ASR controller parameters is proposed to speed up the speed and accuracy of parameter tuning. First of all, the block diagram of the motor speed loop system is simplified to Fig.5 based on the speed loop control rate of PI.

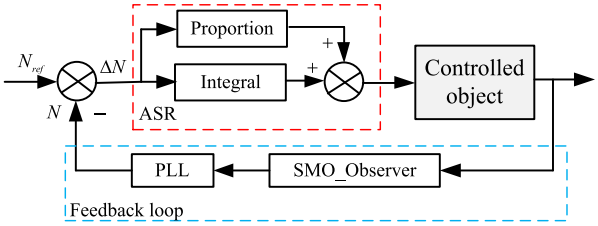

FIGURE 5. The control block diagram of PMSM speed loop.

From Fig.6, the speed loop PI control consists of a proportional coefficient and an integral coefficient (K_p, K_i). The speed error (ΔN) tends to zero when the control system converges. An optimization control system based on PSO is established by utilizing the speed error (ΔN). The block diagram of the parameter-optimized control system is shown in Fig.6. Secondly, aiming to further measure the control

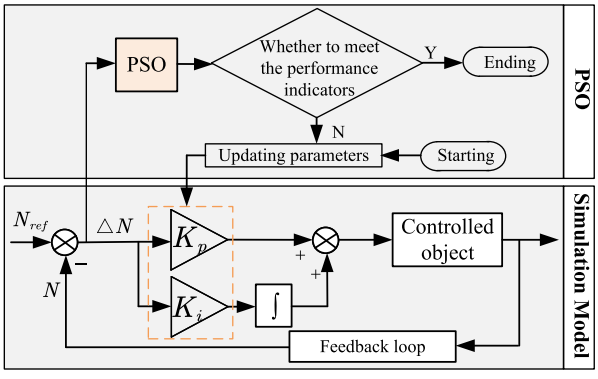

FIGURE 6. The block diagram of PMSM speed loop parameter optimization system based on PSO.

performance of speed loop, the error performance indicator of ITAE (integrated time absolute error) is introduced as the speed controller performance indicator. The performance indicator of ITAE is defined in Eq.(18). On this basis, the minimum value of the performance indicator is utilized as the objective for the optimization of the controller parameters, which indicates that the optimal parameters of speed loop can be searched for by this optimization algorithm.

$$J = \int_0^\infty t\,|e\,(t)|dt \tag{18}$$

where, $e(t)$ represents the speed error, and J denotes the error performance indicators. The performance metrics in this system require to be calculated in a discrete manner.

In Fig.6, the PSO module calculates the better speed loop parameters (K_p, K_i) by collecting the speed error as a way to achieve improved control system performance.

Finally, the velocity-position model is employed to build the particle swarm algorithm during the design of PSO algorithm. The design steps of the algorithm mainly include: generating random particles in D-dimensional space, initializing the search position and velocity, local search, global variable speed, and global search. The velocity-position update equation followed by the global variable speed link is shown in Eqs.(19) and (20).

$$v_{iq}^{t+1} = v_{iq}^{t} + c_1 r_1 (p_{iq}^{t} - x_{iq}^{t}) + c_2 r_2 (p_{iq}^{t} - x_{iq}^{t}) \tag{19}$$

$$x_{iq}^{t+1} = x_{iq}^{t} + v_{iq}^{t+1} \tag{20}$$

where, r_1 and r_2 are random factors between 0 and 1. c_1 and c_2 are speed optimization factors, taking the empirical value of 0.2.

When the velocity-position update equation is incorporated, the parameter optimization model based on PSO adopts the speed error performance metric to measure the merit of the speed loop parameters. During the search process, the velocity-position formula is utilized to update the PI parameter search direction and velocity, thus realizing the parameter variable speed search, speeding up the controller design and optimizing the system performance. Eventually, its optimal speed loop PI parameters are denoted as K_{pASRO} and K_{iASRO} by parameter optimization, respectively.

III. SYSTEM SIMULATION AND RESULTS ANALYSIS

A. THE OVERALL STRUCTURE AND PARAMETER SETTING OF SYSTEM

In this paper, the whole three-phase PMSM system adopts vector control, whose structure mainly includes SVPWM, spatial decoupling transformation and voltage-current double closed-loop control. Secondly, the Hall fault diagnostic module is designed to detect sensor health status and is applied to implement fault-tolerant control system switching. Subsequently, the module of sliding mode observer and the module of phase-locked loop are designed to obtain rotor speed and position acquisitions when the system is in fault-tolerant control. Finally, the scheme of parameter optimization based PSO is proposed to optimize the system fault-tolerant control performance from the speed loop.

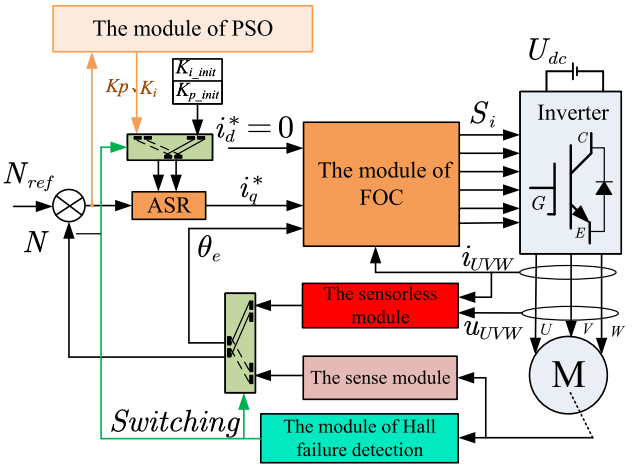

FIGURE 7. The block diagram of Hall fault-tolerant control system based on PSO parameter optimization.

The block diagram of the entire fault-tolerant control system is shown in Fig.7. Furthermore, the Hall fault-tolerant control system of three-phase PMSM proposed in this paper is deployed on the real-time operation platform (RCP-HIL) for system reliability verification.

The parameters of the fault-tolerant control system are shown in Tab.3. In addition, the optimization factors in the particle swarm optimization algorithm have been presented in Section II.

B. SYSTEM SIMULATION AND ANALYSIS BASED ON DIFFERENT OPERATING CONDITIONS

In this paper, the semi-physical platform (HIL-RCP) is employed to perform performance verification experiments of fault-tolerant control system, which is also called hardware-in-the-loop experiment. The connection principle of the platform is shown in Fig.8, and the physical device is shown in Fig.9.

From Fig.8, the system mainly consists of a controller (RCP), a motor simulator (HIL), upper computers and a signal connection board. The PMSM model is burned in the HIL, the control algorithm is burned in the RCP, and the

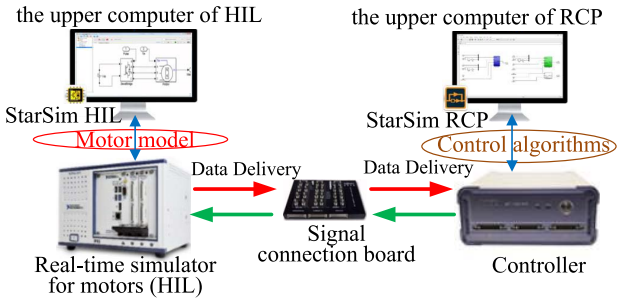

FIGURE 8. The connection principle of semi-physical platform(RCP-HIL).

TABLE 3. The parameters of PMSM and control system.

Three-phase PMSM parameters					
Symbol	Parameter	Value	Symbol	Parameter	Value
P_n	Number of pole pairs	3	L_q/L_d	Equivalent inductance in the dq-coordinate system	0.0085H
J	Moment of inertia	0.008kg.m^2	ψ	Rotor flux	0.3Wb
n^*	Rated speed	1000rpm(r/min)	F	Motor damping coefficient	0.008N·m·s
U_{dc}	DC supply voltage	311V	R	Stator phase resistance	2.875Ω
Control system parameters					
K_{pASRO}	Fault tolerant state velocity loop scaling factor	0.035	f_{pwm}	Carrier frequency	10kHz
K_{iASRO}	Fault tolerant state velocity loop integral coefficient	0.05	K_{pPLL}	Phase-locked loop scaling factor	0.35
K_{pdqACR}	Current loop scaling factor	0.5	K_{iPLL}	Phase-locked loop integral coefficient	25
K_{idqACR}	Current loop integral coefficient	30	T_{sc}	Controller step size	10^{-4}s
K_{pASR}	Normal state speed loop proportional coefficient	1	k	Sliding mode gain factor	350
K_{iASR}	Normal state speed loop zai1 integral coefficient	1	T_{sm}	Simulator step size	10^{-6}s

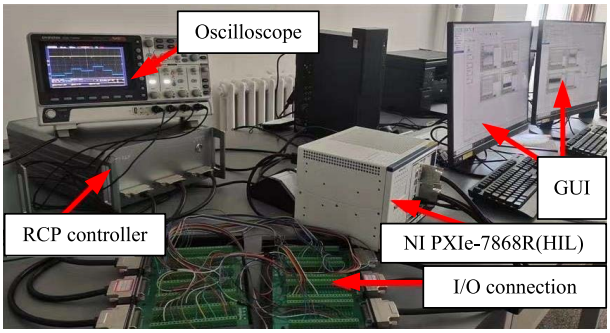

FIGURE 9. The physical installations of semi-physical platform(RCP-HIL).

signal adapter board serves as a data connection between the motor model and the control algorithm. Among them, RCP acts as a real controller to run the control algorithm in real time; and HIL is a real-time simulation hardware for motors developed based on Simulink. It is worth noting that the variable-step-based computing model is deployed to this platform to simulate the actual motor operation more realistically. Therefore, the controller step size (resp. main circuit step size) is set to T_{sc}(resp. T_{sm}). The other control parameters of the fault-tolerant control system are shown in Tab.3. In addition, the device can display the curves of each parameter during system operation in real time directly through the upper computer, which means that all experimental waveforms belong to real time curves.

In order to verify the reliability and performance of the fault-tolerant system, the experiments are implemented from four aspects: the observer response in the fault-tolerant state, the performance of variable-speed control, the performance of variable-load control, and the fault-tolerant control error. Therefore, this subsection is divided into three parts to simulate and validate the established fault-tolerant control system.

1) THE PERFORMANCE ANALYSIS OF FAULT DETECTION MODULE

In order to verify the effectiveness of the Hall fault detection module, the system runs at 800rpm, applies a load of 5$N \cdot m$ at 1s, and then sets A-phase and B-phase Halls to low-level faults at 1.5s, respectively.

Fig.10 illustrates the results of A/B-phase Hall fault detection and the three-phase Hall output waveforms, which reveals that the fault detection module can effectively detect A/B-phase Hall set low-level faults and issue switching commands up within 2/3 electrical cycles (2/3T). Other single-phase Hall faults can also be detected accurately and are not described here.

Furthermore, Fig.11(a)-(b) demonstrate the system speed response waveforms before and after the speed loop parameter update, which shows that the system with updated speed loop parameters is better able to maintain system stability during fault-tolerant state switching. Conversely, the system that has not updated its parameters may go out of control. Hence, the reliability of the proposed fault detection strategy and the superiority of the controller parameter update can be demonstrated from the above experiments.

2) FAULT-TOLERANT CONTROL RESPONSE PERFORMANCE ANALYSIS

After verifying the reliability of the fault detection module, the relative performance of the slip mode observer should also be further verified. It is shown that in Fig.12 the response curves of the observed values of rotor speed and angle when the observer is activated.

From Fig.12(a-b), it can be clearly seen that the strategy in this paper can converge to the actual value in 0.4s and achieve no static difference observation after stabilization.

Furthermore, a switch is designed in the control model to simulate the fault-tolerant switching signal from the Hall fault detection module. The system switches from a sensed control

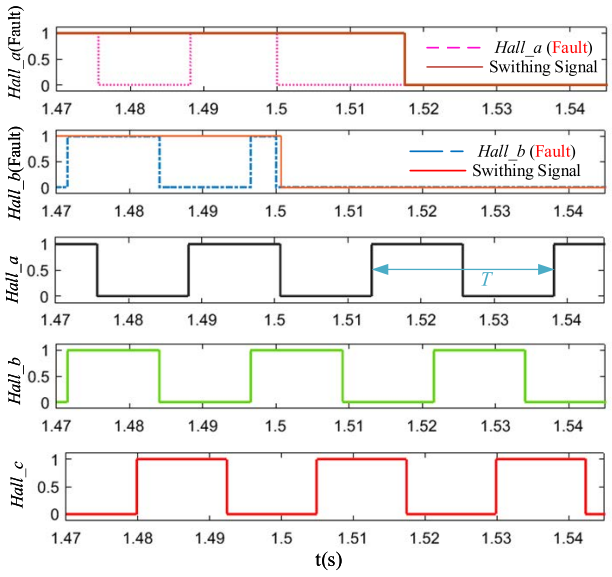

FIGURE 10. The experimental curve of A/B-phase Hall fault detection.

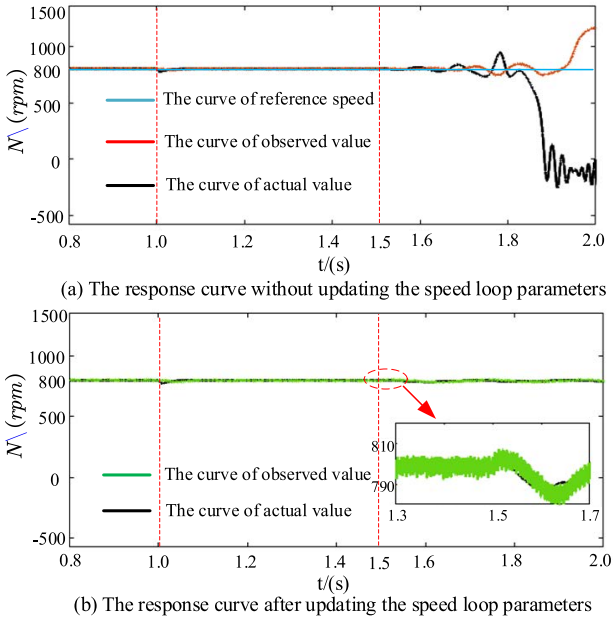

FIGURE 11. The system speed response curve before and after updating the speed loop parameters.

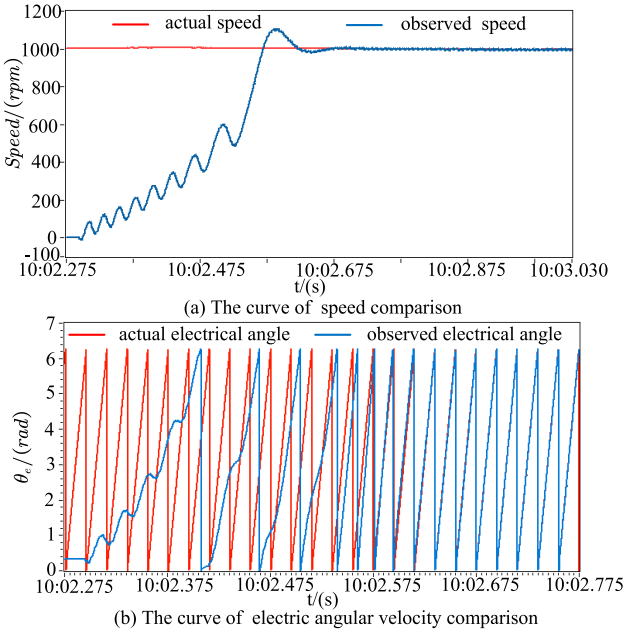

FIGURE 12. The observation and actual value comparison curve under observer open-loop.

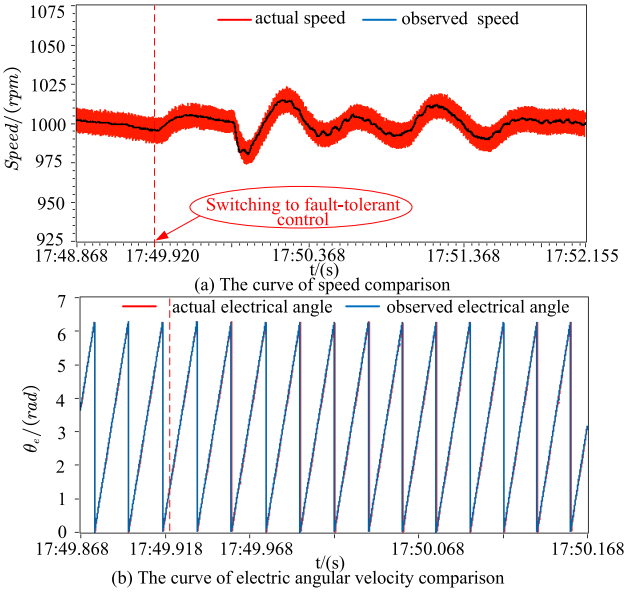

FIGURE 13. The observation and actual value comparison curve under observer close-loop.

state to a fault-tolerant vacant state when the switch that simulates the fault-tolerant switching signal is toggled. The real-time curves of the velocity response and electrical angle observations in the fault-tolerant control state are shown in Fig.13(a-b).

Assuming that the system is switched to sensorless fault-tolerant control state, it is worth noting that a slight fluctuation in speed occurred from Fig.13(a). However, the speed remains near the given speed and stabilizes to the given speed after a slight fluctuation. Furthermore, speed fluctuations occur because the speed feedback loop has changed and the PI parameters of ASR have been re-adjusted, when switching to the fault-tolerant control state. Moreover, the discontinuity term ($sgn(x)$) in the observer fundamentally introduces jitter to the observed values. In addition, the controller model discretization process is also responsible for the weight of the system speed jitter. Note that, the output jitter caused by discrete control can be improved by increasing the controller sampling and operating frequency. However, the operating

frequency of control algorithm is also limited by the master controller frequency as well as the sampling process time.

Most importantly, the fault-tolerant control system still guarantees good real-time angular observation performance during observer closure from Fig.13(b).

3) LOAD PERFORMANCE ANALYSIS UNDER FAULT-TOLERANT CONTROL

A load response test is carried out to verify the load performance of the system under fault-tolerant operation. The load response curve in fault-tolerant control state is shown in Fig.14(a-d).

When the system enters fault-tolerant control, the load of the motor is successively loaded from no load to $5N \cdot m$, then to $10N \cdot m$, and finally reduced back to $5N \cdot m$. It is clear that the fault-tolerant system is able to operate normally with load and respond well to system load variations when tested under variable load in the state of fault-tolerant from Fig.14(a). According to Fig.14(b), the speed of the PMSM in the fault-tolerant control state causes fluctuations in speed both at the moment of loading and load shedding. Nevertheless, the actual speed is also able to recover to the given speed within 2s. Meanwhile, the observed speed also accurately follows the actual value during speed fluctuations.

Furthermore, the estimated rotor electrical angle accurately follows the actual value during the motor switching from stage A to stage B from Fig.14(c). Moreover, the slight error in the estimated value occurs only at the moment of loading. The rotor position curve and the motor current curve also show that the electrical angle period and the phase current period correspond strictly.

Finally, Fig.14(d) shows that the three-phase current exhibits a smooth sinusoidal characteristic during the variable load of stage B to C. In the meantime, the current is able to reach a steady state within $0.2s$ after a slight amplitude fluctuation.

Overall, the accuracy of the rotor position and speed estimation of the system in the fault-tolerant control state is verified through variable load test experiments, and the stability of the fault-tolerant control system is also verified.

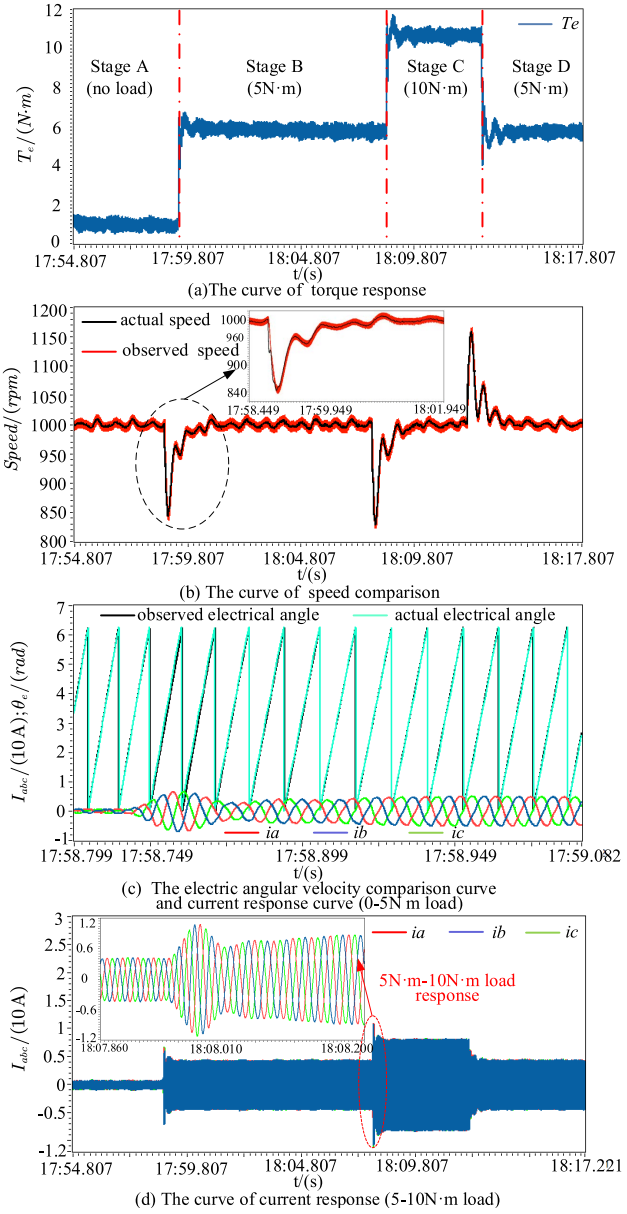

FIGURE 14. The curve of load response in the control state of fault-tolerant(0-5-10-5N·m).

4) THE ANALYSIS OF SPEED RESPONSE PERFORMANCE IN FAULT-TOLERANT CONTROL STATE

After the load disturbance test is carried out, the accuracy of the speed observer and the speed response performance in the fault-tolerant control state are also worthy of attention. Therefore, the variable speed test is carried out under a load of $5N \cdot m$, and the set speed is accelerated from the rated speed ($1000rpm$) to $1200rpm$, and then the speed is reduced to the rated speed after stabilization, and finally the speed is reduced to $800rpm$. The comparison curves and error curves of observed speed and actual speed in the fault-tolerant control state are shown in Fig.15(a-b), during the variable speed and variable load test.

Fig.15(a) records the whole process of the system putting into the observer, switching to the fault-tolerant control state, changing the load and changing the speed in real time. The state of system at each switching time is shown in detail in Tab.4. It clearly reveals that the observed rotor speed accurately follows the actual value when the system is in observer open-loop, observer closed-loop variable-load and observer closed-loop variable-speed operating conditions. Of course, the phenomenon of system output speed jitter is related to the non-continuous term in SMO. Meanwhile, the system responds reasonably well to the speed given value through the variable speed test in the fault-tolerant control.

The speed error curves in Fig.15(b) reflect the accuracy of the observed results under variable load and variable speed operation conditions. The speed observation error can be kept

TABLE 4. System state parameters at each switching time.

Time	t_0(Puting the observer)	t_1(Entering fault-tolerant control state)	t_2	t_3	t_4	t_5	t_6	t_7
Speed (rpm)	1000	1000	1000	1000	1000	1200	1000	800
Load torque (N.m)	No load	0	5	10	5	5	5	5

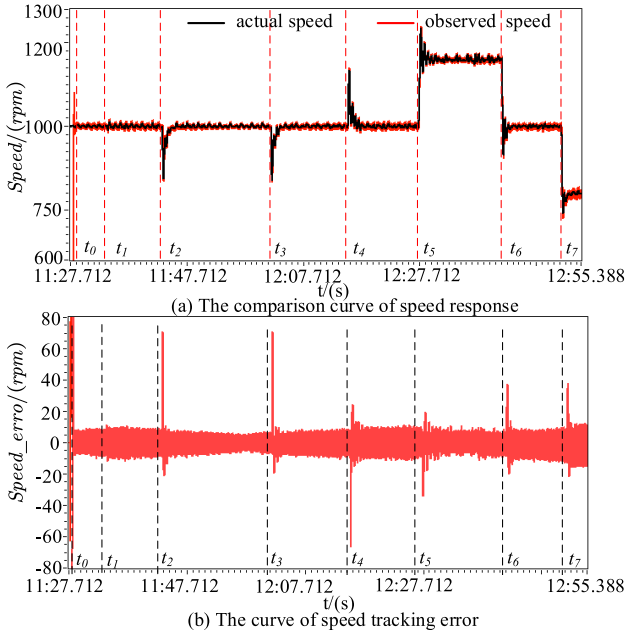

FIGURE 15. The curve of speed response in fault-tolerant control state.

within $\pm 10rpm$ at the steady state of the system. However, it also shows that the observer generates large observation errors for sudden changes in load and sudden changes in speed given. Especially, the speed observer has an estimation error of nearly $70rpm$ when the system is loaded at $5N \cdot m$. In contrast to the loading response, the observer does not produce an estimation error of more than $\pm 30rpm$ during variable speed and load shedding. In general, the speed estimation errors due to variable load and variable speed operation do not impose a significant burden on the control system for systems operating at medium to high speeds. Simultaneously, the observer responds quickly to sudden changes in operating conditions, which makes the estimation error converge quickly.

In summary, the fault-tolerant control method under Hall fault can successfully achieve the response of variable speed and variable load under fault-tolerant condition in the medium and high speed stage, thus maintaining the continuous operation of the system under Hall fault condition and improving the reliability of the system.

C. OBSERVER ROBUSTNESS AND APPLICABILITY ANALYSIS

Firstly, the system with perturbed parts is established according to the equation (Eq.(9)) as in Eq.(21) to analyze the robustness of the SMO.

$$\dot{x}(t) = (A + \Delta A)\, x(t) + (B + \Delta B)\, u(t) + F(t) \tag{21}$$

where, $x(t)$ is the state variable, and $\dot{x}(t)$ is its derivative. A is the state matrix; B is the input matrix. ΔA and ΔB are the ingestion terms; $F(t)$ is an external perturbation term, respectively. Futhermore, the equation of sliding surface (Eq.(11)) is re-derived with the perturbation of this system to obtain Eq.(22).

$$\begin{aligned} \dot{s} &= \frac{\partial s}{\partial x}\dot{x} \\ &= \frac{\partial s}{\partial x}(A + \Delta A)\, x + \frac{\partial s}{\partial x}(B + \Delta B)\, u + \frac{\partial s}{\partial x}F \end{aligned} \tag{22}$$

When the observer converges, $\dot{s} = 0$ is satisfied. Assuming $\det\left(\frac{\partial s}{\partial x}(B + \Delta B)\right) \neq 0$, the equivalent control rate of Eq.(21) can be derived in Eq.(23).

$$u_{eq} = \left[\frac{\partial s}{\partial x}(B + \Delta B)\right]^{-1} \frac{\partial s}{\partial x}\left((A + \Delta A)\, x + F\right) \tag{23}$$

If the parameter uptake of the system satisfies the condition of Eq.(24), the state space expression of the controlled system can be re-derived as Eq.(25) by combining Eqs.(21), (23) and (24).

$$\begin{aligned} \Delta A x(t) &= B\Delta\tilde{A} x(t), \\ \Delta B = B\Delta\tilde{B},\ F(t) &= B\tilde{F}(t) \end{aligned} \tag{24}$$

$$\dot{x} = Ax(t) - B\left(\frac{\partial s}{\partial x(t)}B\right)^{-1} \frac{\partial s}{\partial x(t)}Ax(t) \tag{25}$$

It is can be seen from Eq.(25) that the dynamic expression of the observer is independent of the parameter ingestion term and the external perturbation term when the observer is in the sliding mode plane, which implies the robustness of the SMO to parameter ingestion.

On this basis, robustness comparison experiments based on SMO and nonlinear magnetic chain observer are further implemented, and the experimental results are shown in Fig.16. Where, "100%F" and "105%F" represent the values of original magnetic chain constant and the changed magnetic chain constant, respectively. In addition, "-SMO" and "-FLUX" represent the SMO and the nonlinear magnetic chain observer, respectively. It is clearly evident that after a 5% change in the magnetic chain constant. The observed values of SMO are almost unchanged compared to the nonlinear magnetic chain observer, which indicates that SMO has stronger robustness.

Moreover, the low-speed observation performance of the observer is analyzed such that the applicability of the control

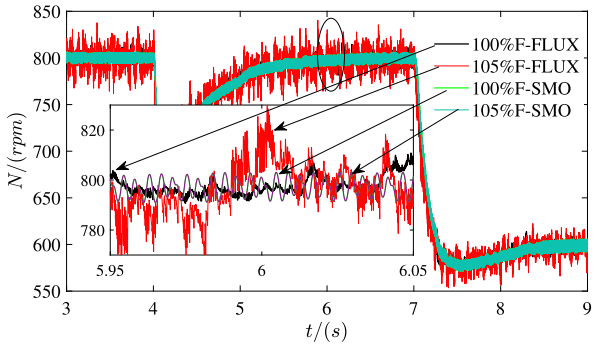

FIGURE 16. The speed curves based on SMO and nonlinear magnetic chain observer.

system of fault-tolerant can be guaranteed. The back-EMF equation is rewritten as shown in Eq.(26).

$$e_d = L_d \frac{di_d}{dt} - \omega_e L_q i_q \tag{26}$$

It can be known from Eq.(26) that the back-EMF of d-axis (e_d) is related to the d-axis, q-axis current and electrical angular velocity. Considering that the system adopts the FOC strategy, the d-axis current reference value is set to 0. Thus, the back-EMF of d-axis is determined by $w_e L_q i_q$.

However, the observer is added with a filter of suitable bandwidth considering that the SMO itself generates high frequency signals. In particular, a sufficiently large back-EMF (much larger than the system noise) is required to ensure effective observation in the actual motor control system. When the motor is started, a large electromagnetic torque is required to overcome the frictional forces and the cogging effect, which means that a large current is generated. More importantly, the motor does not have a speed and the d-axis back-EMF information is not available at the moment of motor startup, which means that the observer remains in an unobservable state. In this circumstance, the observed angle at the moment of motor start is imprecise, which can cause the current that should be applied to the dq-axis to be applied to the observed $\hat{d}\hat{q}$-axis. From Fig.12(b), there is a maximum error of half a cycle between the observed electrical angle and the actual electrical angle in the initial response phase of the observer. If the large current that should be applied to the q-axis is actually applied to the $\hat{q}$-axis during the start-up phase, which can lead to a large observation error and a small effective current component on the q-axis. What's worse, the interior permanent-magnet synchronous motor (IPMSM) is likely to reverse during start-up due to the excessive d-axis current components, by analyzing the electromagnetic torque equation in Eq.(27).

$$T_e = \frac{3}{2} P_n \left[\psi_f + \left(L_d - L_q \right) i_d \right] i_q \tag{27}$$

In addition, excessive current, increased copper consumption, and temperature rise can all be caused when the motor is running at low speeds, which can result in L_d and L_q no longer being constant. It can be seen that the change of the motor parameters can significantly deteriorate the performance of the observer.

Therefore, the fault-tolerant control system proposed in this paper is only for medium and high speed operation conditions, and not for start-up and low speed operation conditions, which is the reason why this system does not consider Hall failure at the start-up moment and low speed operation conditions. If a Hall fault is detected at start-up, a direct shutdown should be considered for repair.

IV. CONCLUSION

Aiming at the problem that the three-phase PMSM Hall sensor is easily damaged during the operation, a fault-tolerant control system based on sensorless state switching is proposed in this paper. Through a large number of variable load and variable speed experiments in the medium and high speed stages, it is proved that the fault-tolerant system can effectively maintain the stable operation of the system and keep good variable load and variable speed response performance in the Hall fault state.

The following list summarizes the key conclusions from this paper.

- A fault-tolerant mode under Hall sensor failure based on sensorless switching is proposed, and the encoded information of the hopping edge of Hall signal is utilized to detect the Hall failure state and switch the control mode.
- When the system is cut into the fault-tolerant control program based on the SMO, the speed loop controller parameter optimization module based on the PSO algorithm is designed with the speed control error minimization as the optimization objective, which speeds up the calculation process of feasible solutions of the controller parameters and ensures the stability of the system after it is cut into the fault-tolerant state.
- Finally, the range of applicability of the fault-tolerant control method and the robustness of SMO proposed in this paper are discussed for medium and high speeds, respectively. Therefore, in future work, low-speed sensorless control, zero-speed sensorless start-up and full-speed fault-tolerant control of three-phase PMSM should be further considered for various industrial environments.

REFERENCES

[1] P. Gao, G. Zhang, and X. Lv, "Model-free control using improved smoothing extended state observer and super-twisting nonlinear sliding mode control for PMSM drives," *Energies*, vol. 14, no. 4, pp. 922–936, 2021.

[2] J. Yan, H. Wang, S. Huang, and Y. Lan, "Load disturbance observer-based complementary sliding mode control for PMSM of the mine traction electric locomotive," *Int. J. Fuzzy Syst.*, vol. 21, no. 4, pp. 1051–1058, Jun. 2019.

[3] Z. Zhang, R. Ma, L. Wang, and J. Zhang, "Novel PMSM control for anti-lock braking considering transmission properties of the electric vehicle," *IEEE Trans. Veh. Technol.*, vol. 67, no. 11, pp. 10378–10386, Nov. 2018.

[4] L. Li, J. Xiao, Y. Zhao, K. Liu, X. Peng, H. Luan, and K. Li, "Robust position anti-interference control for PMSM servo system with uncertain disturbance," *CES Trans. Electr. Mach. Syst.*, vol. 4, no. 2, pp. 151–160, Jun. 2020.

[5] X. Zhang, Y. Zhao, H. Lin, S. Riaz, and H. Elahi, "Real-time fault diagnosis and fault-tolerant control strategy for Hall sensors in permanent magnet brushless DC motor drives," *Electronics*, vol. 10, no. 11, 2021, pp. 1268–1290.
[6] L. Dong, J. Jatskevich, Y. Huang, M. Chapariha, and J. Liu, "Fault diagnosis and signal reconstruction of Hall sensors in brushless permanent magnet motor drives," *IEEE Trans. Energy Convers.*, vol. 52, no. 2, pp. 1542–1554, Mar. 2016.
[7] A. D. Papathanasopoulos, K. N. Giannousakis, E. S. Dermatas, and E. D. Mitronikas, "Vibration monitoring for position sensor fault diagnosis in brushless DC motor drives," *Energies*, vol. 14, no. 8, pp. 2248–2271, 2021.
[8] D. Lv, S. Li, and Z. Du, "Easy Hall position sensor fault-tolerant control algorithm for brushless DC drives," *IEICE Electron. Exp.*, vol. 16, no. 6, pp. 1–11, 2019.
[9] A. Muhammad and J. Hur, "Multiple sensor fault detection algorithm for fault tolerant control of BLDC motor," *Electronics*, vol. 10, no. 9, 2021, pp. 1038–1055.
[10] Y. Shi, Z. Wu, K. Zhi, and J. Xiong, "A simple approach to detect and correct signal faults of Hall position sensors for brushless DC motors at steady speed," *IOP Conf. Mater. Sci. Eng.*, vol. 339, no. 1, 2018, pp. 12004–12009, doi: 10.1088/1757-899X/339/1/012004.
[11] Z. Song, J. Li, M. Ouyang, J. Gu, X. Feng, and D. Lu, "Rule-based fault diagnosis of Hall sensors and fault-tolerant control of PMSM," *Chin. J. Mech. Eng.*, vol. 26, no. 4, pp. 813–822, Jul. 2013.
[12] G. Wang, M. Valla, and J. Solsona, "Position sensorless permanent magnet synchronous machine Drives—A review," *IEEE Trans. Ind. Electron.*, vol. 67, no. 7, pp. 5830–5842, Jul. 2020.
[13] S. Singh, A. N. Tiwari, and S. N. Singh, "Speed and position estimation for sensorless control of PMSM: A critical review," *Recent Adv. Electr. Electron. Eng. Formerly Recent Patents Electr. Electron. Eng.*, vol. 13, no. 6, pp. 804–822, Nov. 2020.
[14] Z. Zhang, "Sensorless control of synchronous machines using fundamental back-EMF voltage—A review," *IEEE Trans. Power Electron.*, vol. 37, no. 9, pp. 10290–10305, Mar. 2022.
[15] M. Hinkkanen, S. E. Saarakkala, H. A. A. Awan, E. Molsa, and T. Tuovinen, "Observers for sensorless synchronous motor drives: Framework for design and analysis," *IEEE Trans. Ind. Appl.*, vol. 54, no. 6, pp. 6090–6100, Nov. 2018.
[16] T. Wang, J. Huang, M. Ye, J. Chen, W. Kong, M. Kang, and M. Yu, "An EMF observer for PMSM sensorless drives adaptive to stator resistance and rotor flux linkage," *IEEE J. Emerg. Sel. Topics Power Electron.*, vol. 7, no. 3, pp. 1899–1913, Sep. 2019.
[17] X. Song, J. Fang, B. Han, and S. Zheng, "Adaptive compensation method for high-speed surface PMSM sensorless drives of EMF-based position estimation error," *IEEE Trans. Power Electron.*, vol. 31, no. 2, pp. 1438–1449, Feb. 2016.
[18] W. Xu, Y. Jiang, C. Mu, and F. Blaabjerg, "Improved nonlinear flux observer-based second-order SOIFO for PMSM sensorless control," *IEEE Trans. Power Electron.*, vol. 34, no. 1, pp. 565–579, Jan. 2019.
[19] W. Cui, S. Zhang, and Y. Feng, "Improved sensorless control scheme for PMSM based on high-frequency square-wave voltage injection considering non-linear change of inductance in D-Q axis," *AIP Adv.*, vol. 11, no. 1, pp. 1–5, 2021.
[20] D. Johnson-Chyzhykov and G. Menon, "Low-speed position sensorless control of IPMSM based on high frequency signal injection," *Electr. Mach. Control*, vol. 22, no. 3, pp. 88–94, 2018.
[21] W. K. Wibowo and S.-K. Jeong, "Improved estimation of rotor position for sensorless control of a PMSM based on a sliding mode observer," *J. Central South Univ.*, vol. 23, no. 7, pp. 1643–1656, Jul. 2016.
[22] Z. Xu, T. Zhang, Y. Bao, H. Zhang, and C. Gerada, "A nonlinear extended state observer for rotor position and speed estimation for sensorless IPMSM drives," *IEEE Trans. Power Electron.*, vol. 35, no. 1, pp. 733–743, Jan. 2020.
[23] C. Gong, Y. Hu, J. Gao, Y. Wang, and L. Yan, "An improved delay-suppressed sliding-mode observer for sensorless vector-controlled PMSM," *IEEE Trans. Ind. Electron.*, vol. 67, no. 7, pp. 5913–5923, Jul. 2020.
[24] S. K. Kommuri, S. B. Lee, and K. C. Veluvolu, "Robust sensors-fault-tolerance with sliding mode estimation and control for PMSM drives," *IEEE/ASME Trans. Mechatronics*, vol. 23, no. 1, pp. 17–28, Feb. 2018.
[25] H. Mesloub, M. T. Benchouia, A. Goléa, N. Goléa, and M. E. H. Benbouzid, "A comparative experimental study of direct torque control based on adaptive fuzzy logic controller and particle swarm optimization algorithms of a permanent magnet synchronous motor," *Int. J. Adv. Manuf. Technol.*, vol. 90, nos. 1–4, pp. 59–72, Apr. 2017.
[26] G.-J. Tan, M.-W. Qian, H. Zhang, Z.-X. Ma, and R.-W. Yu, "Design of robust controller for PMSM based on improved PSO algorithm," *Int. Rev. Electr. Eng.*, vol. 6, no. 5, pp. 2351–2360, 2011.
[27] R. A. Ordonez and C. Hernandez, "Modeling and control of a PMSM motor," *J. Eng. Appl. Sci.*, vol. 12, no. 17, pp. 4514–4525, 2017.
[28] G. Huang, E. F. Fukushima, J. She, and C. Zhang, "Current sensor fault diagnosis based on sliding mode observer for permanent magnet synchronous traction motor," in *Proc. IEEE 27th Int. Symp. Ind. Electron. (ISIE)*, Jun. 2018, pp. 835–840.
[29] J.-S. Chiou, S.-H. Tsai, and M.-T. Liu, "A PSO-based adaptive fuzzy PID-controllers," *Simul. Model. Pract. Theory*, vol. 26, pp. 49–59, Aug. 2012, doi: 10.1016/j.simpat.2012.04.001.

YI HUANG was born in Sichuan, China, in 1998. He received the B.S. degree from Shihezi University, Xinjiang, in 2021, where he is currently pursuing the degree in mechanical engineering with the School of Mechanical and Electrical Engineering. His research interests include motor control, fault tolerant control, sensorless control, and their applications.

MI ZHAO was born in Shihezi, Xinjiang, China, in 1980. She received the B.S., M.S., and Ph.D. degrees from Xidian University, Xi'an, China, in 2002, 2006, and 2009, respectively. She is currently a Professor with the College of Machinery and Electricity. She has authored or coauthored over 20 publications. She has coauthored the book *Optimal Supervisory Control of Automated Manufacturing Systems*. Her research interests include modeling, analysis and control of smart grids, and supervisory control of discrete event systems.

JIAN ZHANG was born in Fukang, China, in 1998. He received the B.S. degree from Shihezi University, Xinjiang, in 2020, where he is currently pursuing the master's degree. His research interests include supervisory control of discrete event systems and artificial intelligence algorithms and their applications.

MIN LU received the B.S. degree in control engineering from Xinjiang University, Xinjiang, China, in 2008, and the Ph.D. degree in electrical engineering from the Huazhong University of Science and Technology, Wuhan, China, in 2020. She is currently a Professor with Shihezi University. She is mainly engaged in the reliability research of power electronics devices and the wind power generation technology.